Electronic Supplementary Material (ESI) for Soft Matter.

Supplementary Information:

Peeling from a liquid

Deepak Kumar[1], Nuoya Zhou[2], Fabian Brau[3], Narayanan Menon[2], and Benny Davidovitch[2]

[1] *Department of Physics, Indian Insitute of Technology Delhi, New Delhi 110016;*

[2] *Department of Physics, University of Massachusetts Amherst, Amherst MA 01003;*

[3] *Nonlinear Physical Chemistry Unit,*

Université libre de Bruxelles (ULB), CP231, 1050 Brussels, Belgium

I. EXPERIMENT

A. Additional data for the translationally symmetric geometry

The data presented in Fig. 2 C and D of the main text correspond to situation where the meniscus has been allowed to relax to near-equilibrium configuration. However, when the film is pulled out from the liquid surface or allowed to absorb on to it at small velocity, one obtains two different values of ψ_0 corresponding to advancing and receding configurations. $\kappa(s)$ curve in situations close to the advancing and receding angles for PS film of thickness $t = 2$ μm is shown in Fig. S1 A and Fig. S1 B respectively. The cusp in $\kappa(s)$ at the three phase contact is clearly seen even in these situations with different values of ψ_0.

B. Examining the data analysis protocol

1. *Case I: Smooth curvature*

In order to make sure that no spurious artifact is introduced by the data analysis algorithm adopted, we take a parabolic function $y = 0.7x^2$ (Fig. S2 A) which has a shape (in length units of mm) similar near the origin to the typically measured sheet profile. The

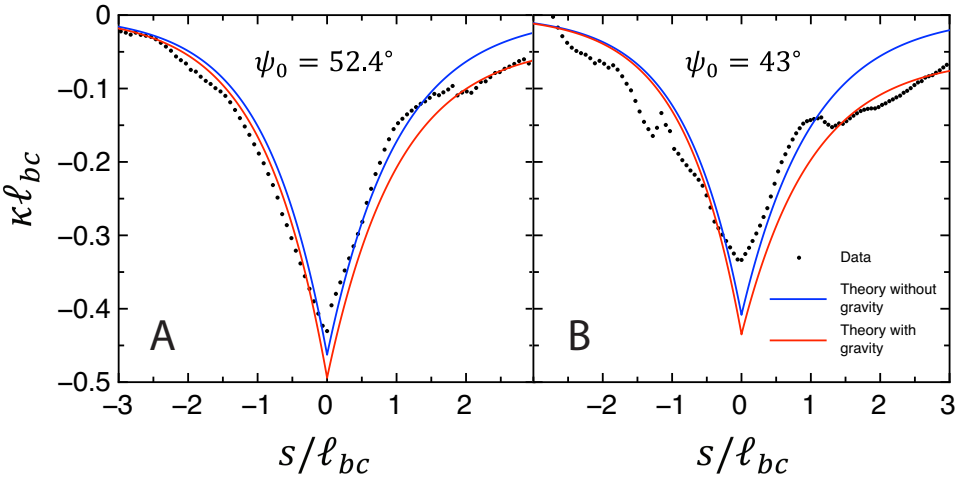

FIG. S1. $\kappa(s)$ for polystyrene film of thickness $t = 2$ μm at (A) $\psi_0 = 52.4°$ close to the advancing configuration and (B) at $\psi_0 = 43°$ close to the receding configuration. The cusp in curvature near the vertex is clearly seen.

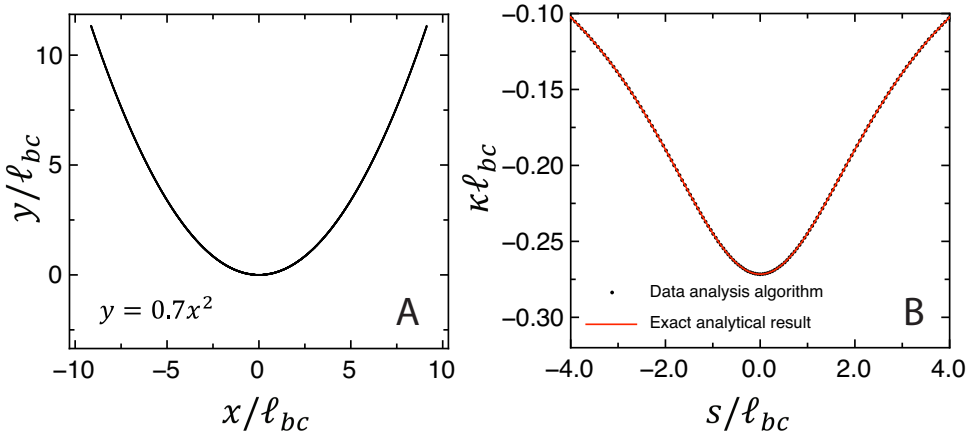

FIG. S2. (A) Data sampled from the function $y = 0.7x^2$. (B) Black circles: Curvature $\kappa(s)$ computed from the data in (A) using the algorithm used in the paper. Red solid curve: $\kappa(s)$ obtained from the function $y = 0.7x^2$ analytically. The two match exactly.

function is sampled to generate (x, y) coordinates. The data set so generated is run through the same algorithm used in the main text to obtain $\kappa(s)$, plotted in Fig. S2B as filled black circles. We have used $\ell_{bc} = 0.2$ mm, a value close to that in the experiments. The exact analytical result obtained for the particular function chosen is plotted as a red solid line. The two match exactly with each other in this case - a parabola has a smooth $\kappa(s)$ curve which the data analysis algorithm captures correctly without introducing any spurious cusp at the origin.

2. Case II: Curvature with a cusp

We consider the following two polynomials:

$$f_1(x) = -0.023x^4 - 0.25x^3 + 0.72x^2 + 0.0023x - 0.0055 \tag{S1}$$

$$f_2(x) = 0.088x^4 + 0.38x^3 + 0.72x^2 + 0.0023x - 0.0055 \tag{S2}$$

Using the above two polynomials we define the following piecewise function:

$$y(x) = \begin{cases} f_1(x) & x < 0 \\ f_2(x) & x > 0 \end{cases} \tag{S3}$$

The coefficients of the polynomials have been chosen to keep the shape (in length units of mm) of the function $y(x)$ similar to a typical experimentally measured profile. The functions

have been plotted in Fig. S3 A (we have assumed $\ell_{bc} = 0.2$ mm). It may be noted that the two polynomials have the same coefficients for the constant, linear and square terms but different coefficients for the cubic and the quartic terms. This implies that at $x = 0$, the function $y(x)$ defined in Eq. (S3) has a continuous but non-smooth curvature. The expected $\kappa(s)$ curve is shown as solid lines in Fig. S3B. The function $y(x)$ in Eq. (S3) is used to generate data points (x, y) at a sampling rate comparable to the experiments. When the data analysis algorithm is employed on the polynomial functions $f_1(x)$ and $f_2(x)$, the curvature (open circles in Fig. S3 B) match exactly with the expected result.

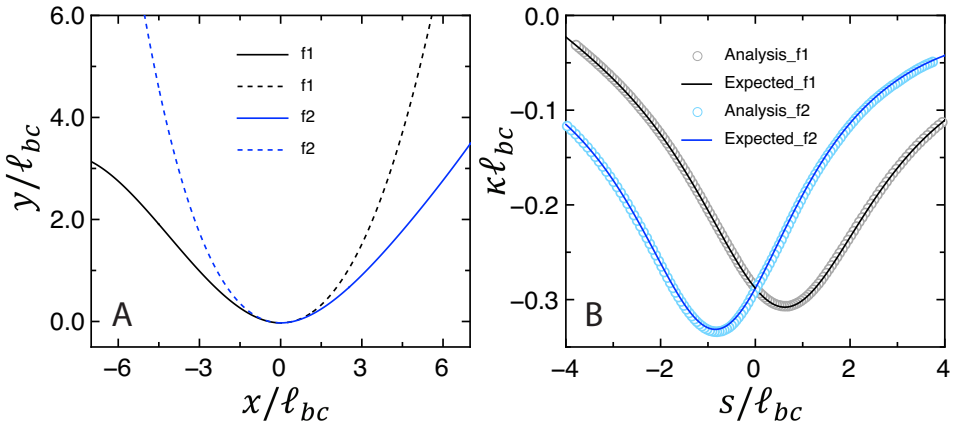

FIG. S3. (A) Two polynomial functions $f_1(x)$ and $f_2(x)$ are used to define a piecewise function $y(x)$ shown as solid line, see Eqs. (S1)-(S3). (B) $k(s)$ curve obtained for the functions $f_1(x)$ and $f_2(x)$ using the data analysis algorithm (open circles) match exactly with the expected result (solid lines).

Curvature was obtained by using our data analysis algorithm on the data generated by sampling the function $y(x)$ is shown in Fig. S4A. The red, blue and green curves show the curvature computed by taking $\Delta = \ell_{bc}$, $0.5\ell_{bc}$ and $0.2\ell_{bc}$ respectively while the black curve shows the analytically calculated result. We next study the effect of noise present in experimentally measured data. In panels B and C of Fig. S4 a uniformly distributed noise of width corresponding to 1 and 5 pixels, respectively, have been added to the function $y(x)$ before sampling it to obtain the data for analysis. We observe that a smaller value of Δ does a better job of reproducing the expected curvature near the vertex in absence of noise. However, in the presence of noise, a larger value of Δ is needed to average out the effect of noise. The value $\Delta = \ell_{bc}$ chosen for the analysis is an good compromise for the typical level

of noise present in the experimental data.

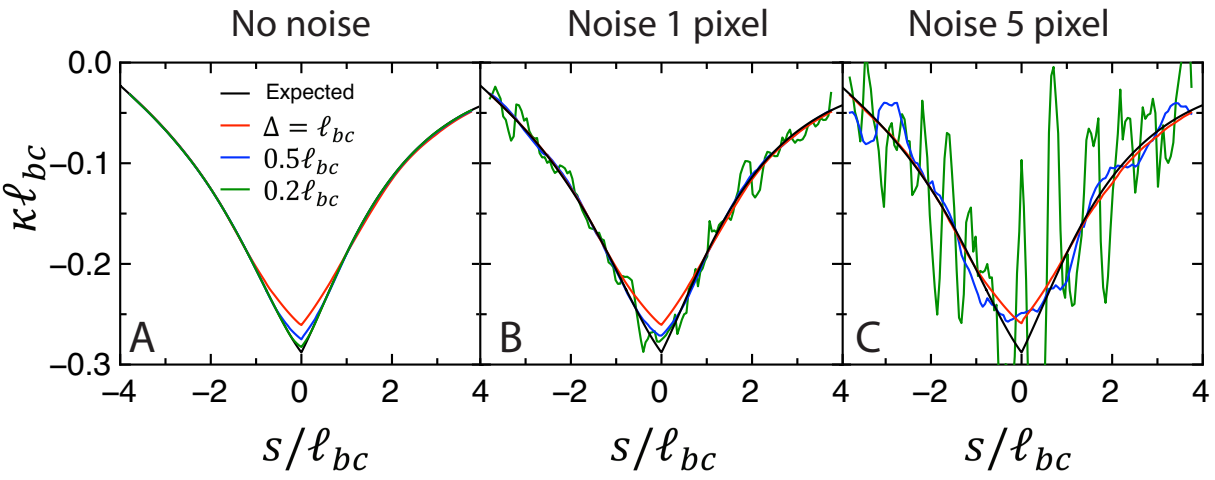

FIG. S4. Effect of varying the value of Δ in the data analysis protocol. Smaller values of Δ give a better match to the expected curvature in the limit of low noise. As the noise in data is increased the curves obtained with lower values of Δ become more noisy. $\Delta \approx \ell_{bc}$ seems to be a good choice for Δ.

As described in the main text, in our data analysis algorithm the data is sampled in a different way for the interval containing the vertex compared to other intervals. In each iteration, we choose one data point randomly with uniform probability from all other intervals, however, from the interval containing the vertex the data point is chosen randomly with a normal probability distribution centered at position of vertex. Fig. S5 shows the significance of this step. If we sample the interval containing the vertex in the same way as other intervals, the position of the cusp varies slightly from iteration to iteration. As a result when the average is calculated the cusp is smoothed out (Fig. S5 blue curve). On the other hand choosing the vertex preferentially reduces this noise and helps in capturing the non-smooth nature of the curvature (Fig. S5 red curve).

C. Experimental details regarding the axially symmetric case

In the axially symmetric case, an air bubble is introduced underneath a thin film floating on water surface to create a three-phase contact line. In order to image the film profile, the polystyrene film is fluorescently tagged with the dye Nile Red. Before spin-coating

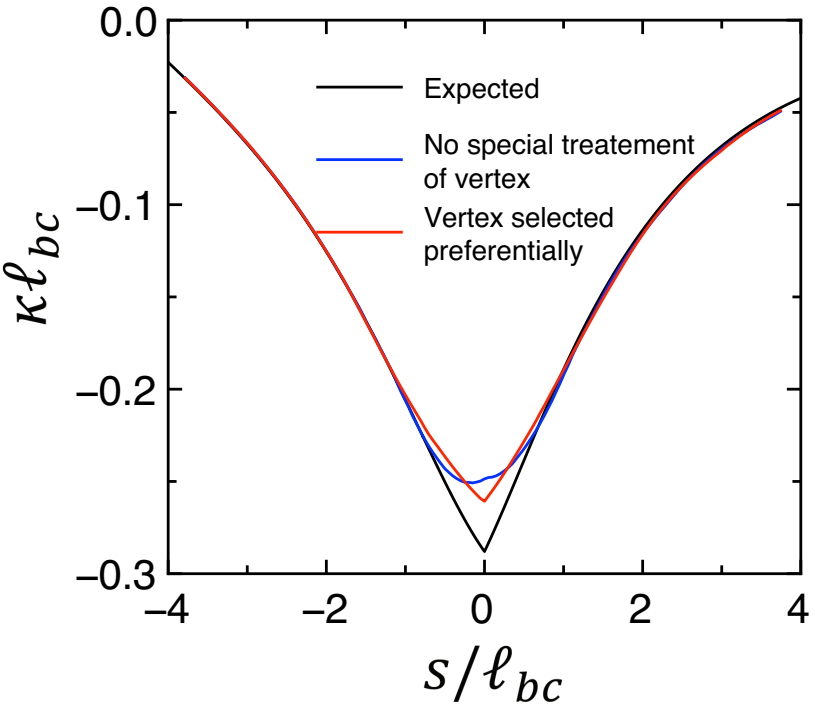

FIG. S5. The blue curve shows the curvature $\kappa(s)$ obtained if we allow each data point in the interval containing the vertex to be chosen with equal probability. We notice that the cusp in the curvature present in the actual function (black curve) is smoothed out. In the data analysis protocol adopted, in the interval containing the vertex, we select points with a normal probability distribution centered at the vertex and having a width comparable to the typical error in the measurement of the vertex (red curve).

polystyrene, Nile Red is dissolved in polystyrene-toluene solution at a concentration of 10^{-6}wt %. After spin coating, we obtain films that can be excited by a sheet of green laser, using a scheme similar to that illustrated in Fig. 2A of the main text, to get the solid-vapor interface. The red-channel of a typical image obtained using this method is shown in Fig. S6A. As can be noticed in the image, the liquid-vapor interface is not visible in this scheme. We, therefore, also capture a bright field image using the same setup under normal room lighting, which reveals the lower part of the air-bubble as shown in Fig. S6 B. In Fig. S6 C, we show an image where Fig. S6 B has been overlayed on Fig. S6 A. The red dashed curve shows a circular curve fitted to the visible part of the air bubble.

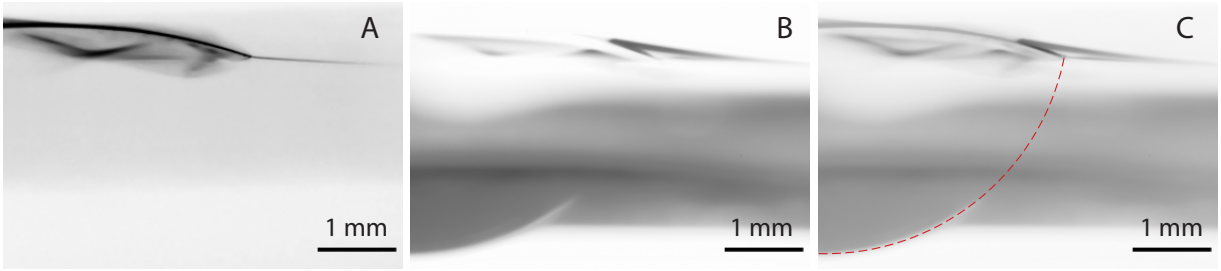

FIG. S6. (A) Image (red-channel) of the film profile in the axially-symmetric geometry obtained using fluorescent imaging. (B) Bright field image capturing a part of the air-bubble. (C) Image B overlayed on image A. The red dashed curve is a circle fitted to the visible part of the air-bubble.

D. Note on error bars in the measurements

In order to compute the curvature, we divide the whole data set into intervals of length Δ and choose one data point from each interval. A spline function of order 3 made up of Hermite polynomials is generated using the data points sampled in each iteration (i) and the curvature $\kappa_i(s)$ is computed on this spline function at every $n^{th}(\sim 10)$ point of the original data. The process is repeated a large number of times (N), selecting a different sampling of data points randomly in each iteration, such that the whole data set is adequately represented. The curvature profiles obtained from individual data samples are averaged to obtain the final $\kappa(s)$ curve: $\kappa(s) = \frac{1}{N}\sum_{i=1}^{N}\kappa_i(s)$. The variance in $\kappa(s)$ is computed as $\sigma_\kappa^2(s) = \frac{1}{N}\sum_{i=1}^{N}(\kappa_i(s) - \kappa(s))^2$. The error bars on $\kappa(s)$ are computed as $\sigma_\kappa(s)/\sqrt{n}$. Fig. 2C of the main text shows the typical error bars measured.

II. THEORY

This part of the SI consists of two subsections. In the first, we describe a variational analysis approach to obtain the force balance, Eq. (9), as an Euler-Lagrange equation, whose solution is an extremum of the energy of the liquid-sheet-vapor system. The variational approach helps to clarify the difference between the discontinuities exhibited in peeling from a liquid subphase, Eq. (3), and a rigid substrate, Eq. (1). The primary purpose of this derivation is to substantiate the origin of the term $\gamma_{lv}\sin\theta_Y\delta_d(s)$ in the force balance equation (9), which was explained in the main text as the normal component of localized

force γ_{lv} exerted at the contact line on the sheet by a liquid-vapor interface of surface tension tilted at an angle θ_Y with the tangent to the sheet's mid-surface. Since this localized force is purely capillary, and does not depend on liquid gravity (which only affects the shape at scales $\sim \ell_c$), we first ignore gravity and address instead a more elementary set-up of a liquid drop of finite volume in contact with a sheet. In the next subsection we elaborate on the solution of the capillary *elastica*, Eq. (9), which is given by Eqs. (11) and (12) and shown as the solid blue curves in Fig. 2B-D (and the correction due to the effect of liquid gravity, shown as red solid curves in Fig. 2C-D and dashed blue in Fig. 2B).

A. Variational analysis

1. Drop on sheet

We consider the energy of an inextensible solid film of length L in contact with a liquid drop. Following Ref. [1], we assume a 1D geometry, where both the sheet (of length L) and the liquid drop (of cross-section area A_0) are infinite in the $\hat{z}$ direction, perpendicular to the plane in Fig. S7A. Retaining the notations of the main text, (but ignoring for now liquid gravity), we denote the shape of the planar cross-section by $\vec{X}(s)$, where $0 < s < L$ is the arclength of the sheet's midsurface, and $\theta(s)$ is the angle between the tangent $\hat{t}(s) = d\vec{X}/ds$ and the horizontal $\hat{x}$ axis. We assume that the sheet is sufficiently long such that the liquid contacts it in a finite interval $\Delta s \equiv s_2 - s_1$, where $0 < s_1 < s_2 < L$. Thus, the variables (degrees of freedom), over which the energy functional $\mathcal{U}$ must be minimized, are the shape $\vec{X}(s)$ of the sheet's midsurface, and the contact coordinates s_1, s_2. We further assume that edges of the sheet are pulled by a tensile load (force/length) T, oriented along the $\hat{x}$ axis.

The total energy per unit length along $\hat{z}$, of the liquid-vapor-sheet system is:

$$\mathcal{U} = \mathcal{U}_{bend} + \mathcal{U}_{surf} - p(\mathcal{A} - A_0) - T\mathcal{D} \tag{S4}$$

Here, the bending energy $\mathcal{U}_{bend}\{\vec{X}(s)\} = \frac{1}{2}B\int_0^L \kappa(s)^2 ds$, where B is the bending modulus and $\kappa(s) = |\hat{n}d\hat{t}/ds|$ is the curvature of the sheet's midsurface, and the surface energy is $\mathcal{U}_{surf}\{s_1, s_2\} = \gamma_{lv}\mathcal{L}_{liq} + (\gamma_{sl} - \gamma_{sv})\Delta s$, where $\mathcal{L}_{liq}$ is the length of the liquid-vapor interface. The third term in Eq. (S4) enforces the liquid volume constraint (which becomes a liquid's cross-sectional area constraint in our 1D geometry), for the area $A\{\vec{X}(s), s_1, s_2\}$ enclosed between the liquid-vapor interface and the sheet, and the pressure p is the corresponding

Lagrange multiplier. The last term is the work done by tensile load T, where $D\{\vec{X}(s)\} \equiv \int_0^L dx = \int_0^L \cos\theta \, ds$ is projection of the sheet's length onto the horizontal axis $\vec{x}$. Note that for clarity, we prescribed the actual variables on which each term in Eq. (S4) depends.

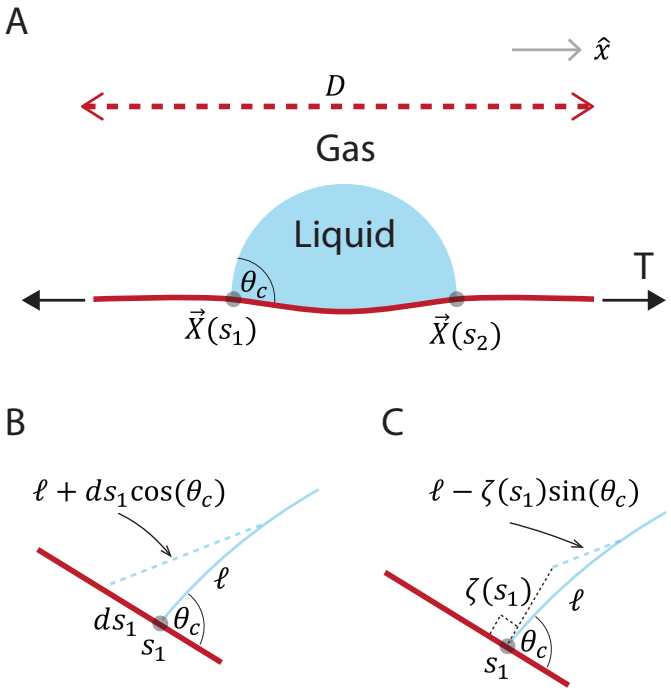

FIG. S7. (A) A schematic figure showing a one-dimensional "drop-on-elastica" configuration, subjected to tensile load, that we address in Sec. (II A 1). (B) Variation of the contact coordinate $s_1 \to s_1 + ds_1$. (C) variation of the shape $\vec{X}(s) \to \vec{X}(s) + \zeta(s)\hat{n}(s)$.

The equilibrium (force balance) equation are:

$$\frac{\delta \mathcal{U}}{\delta s_1} = \frac{\delta \mathcal{U}}{\delta s_2} = 0 \ , \tag{S5}$$

which must be supplemented by the equations that describe the variation of the solid's midsurface's shape, $\vec{X}(s) \to \vec{X}(s) \to \vec{X} + \zeta(s)\hat{n}(s)$, where $\hat{n}(s)$ is the normal to the shape, defined by $\hat{n}\hat{t} = 0 \Longrightarrow \hat{n}(s)\hat{x} = -\sin\theta(s)$:

$$\frac{\delta \mathcal{U}}{\delta \zeta(s)} = 0. \tag{S6}$$

Let us assume now some smooth shape $\vec{X}(s)$, and consider the variation of the energy $\mathcal{U}$, as expressed in Eqs. (S5) and (S6).

The liquid-vapor interface: In fact, the degrees-of-freedom of $\mathcal{U}$ include also the actual shape of the liquid-vapor interface, which determines $\mathcal{L}_{liq}$ and $\mathcal{A}$. However, for a given smooth sheet's shape $\vec{X}(s)$ and contact coordinates s_1, s_2, the minimization of $\gamma_{lv}\mathcal{L}_{liq} - p(\mathcal{A} - A_0)$ reduces to the standard Laplace problem (*i.e.* minimization of the surface area of a fixed volume or the perimeter of a fixed area). This implies that the liquid-vapor boundary is a part of a circle, whose curvature κ_ℓ is determined by the shape $\vec{X}(s)$ in the interval $s_1 < s < s_2$ and the drop's cross-sectional area A_0. This part of the minimization also determines the pressure $p = \gamma\kappa_\ell$, exerted by the liquid drop on the wet part of the sheet.

Eq. (S5): Again, for a given smooth sheet's shape $\vec{X}(s)$, consider variation of s_1 (equivalently s_2), that is – "sliding" the contact line along a given shape of the sheet. Such a variation does not affect $\mathcal{U}_{bend}$ or $T\mathcal{D}$. Furthermore, as Fig. S7B shows, a variation $s_1 \to s_1 + ds_1$ (*i.e.* an infinitesimal ds_1) affects only $O(ds_1)^2$ change to the value of the liquid area functional $\mathcal{A}$ (alternatively, the curvature κ_ℓ). Hence, the only term in Eq. (S4) that undergoes $O(ds_1)$ change is $\delta\mathcal{U}_{surf}$, and Eq. (S5) becomes $\delta\mathcal{U}_{surf}/\delta s1 = 0$. Now, basic trigonometry shows that $\delta\mathcal{U}_{surf} = (\gamma_{sl} - \gamma_{sv} + \gamma_{lv}\cos\theta_c)ds_1$, where θ_c is the contact angle between the liquid-vapor interface and the wet portion of the sheet. Consequently, Eq. (S5) yields the YLD law, $\theta_c = \cos^{-1}\frac{\gamma_{sl}-\gamma_{sv}}{\gamma_{lv}}$. This part of the calculation merely generalizes the classic YLD law (for a liquid drop on a flat, rigid solid surface) to an inextensible solid sheet.

Eq. (S6): We finally turn to variation of the sheet's shape $\vec{X}(s)$. First, the liquid-vapor surface energy, $\gamma_{lv}\mathcal{L}_{liq}$ is affected only by $\zeta(s_1)$ and $\zeta(s_2)$, and using basic trigonometry once again (Fig. S7C) shows that $\delta\mathcal{L}_{liq} = -\gamma_{lv}\sin\theta_c(\zeta(s_1) + \zeta(s_2)) = -\gamma_{lv}\sin\theta_c\int_0^L ds\ \zeta(s)(\delta_d(s - s_1) + \delta_d(s - s_2))$. Second, we have that $\delta\mathcal{A} = \int_{s_1}^{s_2} ds\ \zeta(s)$. Thus, recalling that we proved already $\theta_c = \theta_Y$, we find that $\delta[\gamma_{lv}\mathcal{L}_{liq} - p(\mathcal{A} - A_0)] = \int_0^L ds\ \{-p(s) + \gamma_{lv}\sin\theta_Y[\delta_d(s - s_1) + \delta(s - s_2)]\}$, where $p(s) = \gamma_{lv}\kappa_\ell$ for $s_1 < s < s_2$ and zero othrwise. This is the total capillary force, exerted by the liquid volume and the liquid-vapor interface on the sheet. The analogous terms comprise the RHS of Eq. (9).

Now we consider the variation of the remaining terms in $\mathcal{U}$ with $\zeta(s)$, namely:

$$\frac{1}{2}B\delta\int_0^L ds\ \kappa(s)^2 + (\gamma_{sl} - \gamma_{sv})\delta\int_{s_1}^{s_2} ds - T\delta\int_0^L ds\cos\theta(s)\ . \tag{S7a}$$

Following Ref. [2], we use the following relations:

$$ds \quad \rightarrow \quad ds[1-\kappa(s)\zeta(s)] \tag{S7b}$$

$$\cos\theta(s)=\hat{t}(s)\cdot\hat{x} \quad \rightarrow \quad \hat{t}(s)\cdot\hat{x}+\zeta'(s)\hat{n}(s)\cdot\hat{x}=\cos\theta(s)-\sin\theta(s)\zeta'(s) \tag{S7c}$$

$$\kappa(s) \quad \rightarrow \quad \kappa(s)+\zeta''(s)+\kappa^2(s)\zeta(s)\ . \tag{S7d}$$

Let us discuss the variation of the various terms in Eq. (S7a): *(i)* The first relation, Eq. (S7b), implies intextensibility of the deformation, $\vec{X}(s)\rightarrow\vec{X}(s)+\zeta(s)\hat{n}(s)$, must be supplemented by a constraint, $C\int_0^L\kappa(s)\zeta(s)ds$, where C is a Lagrange multiplier. Notably, the variation $(\gamma_{sl}-\gamma_{sv})\delta\int_{s_1}^{s_2}ds$ only affects the value of the constant C in the wet portion of the sheet, $s_1<s<s_2$; *(ii)* Eqs. (S7b) and (S7c) show that $-T\delta\int_{s=0}^{L}ds\ \cos\theta(s)=0$ (where we used integration by parts); *(iii)* Eqs. (S7b) and (S7d) show that $\frac{1}{2}B\delta\int_0^L ds\,\kappa(s)^2=B\int_0^L ds\,\kappa''(s)+\frac{1}{2}\kappa^3(s)$, where again we used integration by parts.

Combining those pieces together, we find that Eq. (S6) reduces to:

$$B[\kappa''(s)+\frac{1}{2}\kappa^3(s)]-C(s)\kappa(s)=-p(s)+\gamma_{lv}\sin\theta_Y[\delta(s-s_1)+\delta(s-s_2)]\ , \tag{S8}$$

where the pressure $p(s)=\gamma_{lv}\kappa_\ell$ in the wet part, $s_1<s<s_2$ and zero in the dry parts ($0<s<s_1$ and $s_2<s<L$), and $C(s)$ assumes a constant value in each of the 3 segments, $0<s<s_1$, $s_1<s<s_2$, and $s_2<s<L$.

Regardless of the values of integration constants C (which is attributed to the load T exerted on the sheet, as in the classical *elastica* theory), the form of the capillary *elastica* (S8) suffices to prove the jump condition for κ', Eq. (3) of the main text.

2. Peeling sheet from liquid sub-phase

The energy functional for the peeling geometry that is the subject of the main text, differs from Eq. (S4) in some related ways. First, the liquid volume constraint is replaced by the liquid gravitational potential energy. Second, there is only one contact liquid-solid-vapor contact line (taken to be at $s=0$ in the main text). Third, the pulling forces that act on the dry edge (T_{peel} by the peeler) and the wet edge (γ_{lv} due to the liquid-vapor bath) are not identical in magnitude and furthermore acts along different directions (vertical and horizontal, respectively). Nevertheless, these differences do not affect the nature of the localized force $\gamma_{lv}\sin\theta_Y\delta_d(s)$ that act at the contact line, and hence the jump condition,

Eq. (3), remain intact. Furthermore, they do not affect the form of the capillary *elastica*, but only modify the value of the liquid pressure p that act on the wet part of the sheet, and setting the values of the constant C in the dry and wet parts, as described in the main text.

3. Difference from peeling off a rigid substrate

The energy functional, Eq. (S4), includes the energetic contributions due to deformations of the solid sheet and the liquid subphase. The variation of this energies give rise to force balance equation (S8), whose RHS specifies the force exerted on the sheet for any configuration (given by $[\vec{X}(s), s_1, s_2]$). The jump condition (3) is obtained directly from the this force balance equation.

In contrast, when peeling from a rigid substrate the only energetic cost is that of the sheet, while the rigidity of the substrate implies that there is no explicit energetic cost associated with its deformation. Instead, the rigid substrate can exert an arbitrary force on the sheet, such that we do not have here a force balance equation, analogous to Eq. (S8). In this case, the jump condition at the contact line is obtained as a stationarity condition, which balances the work done by moving the contact line a distance ds, and the corresponding energetic costs of bending the sheet $\propto B\kappa^2 ds$. Such a stationarity condition underlies the Obreimoff jump condition, Eq. (1) of the main text (see Ref. [3] for a succinct review of various alternative ways to formally derive this).

B. Solution of the capillary *elastica*

It is useful to address the localized force on the RHS of Eq. (9) by considering it as a "boundary condition" at the contact point $s = 0$ that separates the wet and dry parts of the sheet. Namely, on both sides of the contact line, the profile of the film is determined by Eq. (9). If liquid gravity is ignored, in each of the regions ($s > 0$ and $s < 0$) Eq. (9) can be considered as a nonlinear 3^{rd} order equation (ODE) for the angle $\psi(s)$, whose solution requires 3 boundary conditions (BCs). Eqs. (3) and (10) provide two of those six BCs. In order to specify the other four BCs, we use the normalized arclength and curvature as defined in the main text: $\bar{s} = s/\ell_{bc}$, $\bar{\kappa} = \kappa\ell_{bc}$, and consider the BCs at $\bar{s} \to \pm\infty$. We also rescale the vertical coordinate $\bar{y} = y/\ell_c$ (and note that in the vicinity of the contact line,

i.e. $\bar{s} \sim O(1)$, we have that $\bar{y}(\bar{s}) \approx H_0 + O(\sqrt{\epsilon})$.) In terms of the rescaled variables, Eq. (9) becomes:

$$\left[\bar{\kappa}'' + \frac{\bar{\kappa}^3}{2}\right] - \bar{T}(\bar{s})\bar{\kappa} = -\bar{P}(\bar{s}) + \sin\theta_Y \delta_d(\bar{s})$$

$$\bar{P}(s) = \begin{cases} 0 & \bar{s} < 0 \\ -\sqrt{\epsilon}\bar{y}(\bar{s}) & \bar{s} > 0 \end{cases} \qquad \bar{T}(\bar{s}) = \begin{cases} T_{peel}/\gamma_{lv} & \bar{s} < 0 \\ 1 & \bar{s} > 0 \end{cases} \tag{S9}$$

In the terminology of singular perturbation theory, we seek to provide boundary conditions for Eq. (S9) in the "inner region", $|\bar{s}| \sim O(1)$, by matching to an "outer region", $|\bar{s}| \gg 1$. In the dry part, the film reaches a straight vertical profile, such that: $\psi, \bar{\kappa} \to 0$ as $\bar{s} \to -\infty$. In the wet part, we consider distances $\ell_{bc} \ll s \ll \ell_c$ from the contact line, such that $\bar{s} \sim O(1/\sqrt{\epsilon}) \to \infty$, where we recall that $\epsilon \ll 1$. In this "intermediate" region, the bending-dominated vicinity of the contact line appears as a point (the "vertex"), whereas the curvature due to the the gravity-dominated meniscus is small ($\sim O(\ell_c^{-1})$), such that the surface appears as a slightly curved plane, inclined at an angle $\approx \psi_0$ to the vertical. The normalized curvature, $\bar{\kappa} \approx \sqrt{\epsilon} f(\psi_0)$, where ψ_0 and $f(\psi_0)$ are given by Eq. (7), such that at $O(\epsilon^0)$ the six BCs are:

$$\begin{aligned} \bar{s} \to -\infty \ : \quad & \psi \to 0 \ ; \ \bar{\kappa} \to 0 \\ \bar{s} \to +\infty \ : \quad & \psi \to \psi_0 \ ; \ \bar{\kappa} \to 0 \\ \bar{s} = 0 \ : \quad & [[\bar{\kappa}]] = 0 \ , \ [[\bar{\kappa}']] = -\sin\theta_Y \end{aligned} \tag{S10}$$

Furthermore, at $O(\epsilon^0)$ the hydrostatic pressure in Eq. (S9) is negligible, and the equation becomes integrable. The exact solution, which satisfies all BCs (S10) is given by Eqs. (11) and (12). The tangent angle is readily obtained by integrating the curvature, yielding:

$$\begin{aligned} \bar{s} > 0 \ : \ & \psi = \psi_0 + \pi - 4\tan^{-1}\tanh\frac{\bar{s} + \bar{s}_w}{2} \\ \bar{s} < 0 \ : \ & \psi = -\pi - 4\tan^{-1}\tanh[\frac{\bar{s} + \bar{s}_d}{2}\sqrt{r}] \end{aligned} \tag{S11}$$

To facilitate comparison with experimental data, it is useful to incorporate the effect of liquid gravity, namely, $\bar{P} \sim O(\sqrt{\epsilon})$ in Eq. (S9). When focusing on the "inner" region (*i.e.* vicinity $|s| \lesssim \ell_{bc}$ of the contact line), this amounts to computing the $O(\epsilon)$ corrections to the above $O(\epsilon^0)$ solution. This is obtained by substituting the formal expansion: $\bar{\kappa} = \bar{\kappa}_0 + \sqrt{\epsilon}\bar{\kappa}_1 + \cdots$, in Eq. (S9) where $\bar{\kappa}_0$ is given by Eq. (11), and solving the resulting (linear)

ODE for $\bar{\kappa}_1$ (where the BCs at $\bar{s} \to \infty$ include now the $O(\sqrt{\epsilon})$ terms that were neglected in Eq. (S10)). Even though the relative effect of the correction $\sqrt{\epsilon}\bar{\kappa}_1$ is small in the inner region, where $\bar{\kappa}_0$ is finite, it eventually dominates the curvature in the "outer" region, $\bar{s} \to \infty$, where $\bar{\kappa}_0 \to 0$. Specifically, for $\bar{s} \gg 1$, one finds that the dominant term on the LHS of Eq. (9) is $-\gamma_{lv}\kappa$, whereas the RHS is approximated by $-P \approx \rho g \ell_c f(\psi_0) \approx \sqrt{\rho g \gamma_{lv}} f(\psi_0)$ (where $f(\psi_0)$ is given by Eq. (7)). Consequently, at $\bar{s} \to \infty$ we obtain: $\bar{\kappa} \approx \sqrt{\epsilon}\bar{\kappa}_1 \approx -\sqrt{\epsilon} f(\psi_0)$. This small, finite asymptotic value of the curvature in the wet part of the sheet is readily observed in the red curves in Figs. 2C and 2D, and its effect is noticeable upon comparing the solid and dashed blue curves in Fig. 2B.

---

[1] S. Neukirch, A. Antkowiak, and J.-J. Marigo, The bending of an elastic beam by a liquid drop: a variational approach, Proc. Roy. Soc. A **469**, 20130066 (2013).

[2] D. Mumford, Elastica and computer vision, in *Algebraic Geometry and its Applications: Collections of Papers from Shreeram S. Abhyankar's 60th Birthday Conference* (Springer, 1994) pp. 491–506.

[3] C. Majidi, Remarks on formulating an adhesion problem using euler's elastica (draft), Mech. Res. Com. **34**, 85 (2007).